JACS Au
AN OPEN ACCESS JOURNAL OF THE AMERICAN CHEMICAL SOCIETY

pubs.acs.org/jacsau

Article

Supervalence Bonding in Bi-icosahedral Cores of $[M_1Au_{37}(SC_2H_4Ph)_{24}]^-$ (M = Pd and Pt): Fusion-Mediated Synthesis and Anion Photoelectron Spectroscopy

Emi Ito, Shun Ito, Shinjiro Takano, Toshikazu Nakamura, and Tatsuya Tsukuda*

Cite This: *JACS Au* 2022, 2, 2627−2634

Read Online

ACCESS | Metrics & More | Article Recommendations | Supporting Information

ABSTRACT: $Au_{38}(PET)_{24}$ (PET = SC_2H_4Ph) is known to have a bi-icosahedral Au_{23} core consisting of two Au_{13} icosahedrons by sharing three Au atoms. Previous theoretical studies based on a supervalence bond (SVB) model have demonstrated that the bonding scheme in the Au_{23} core is similar to that in the F_2 molecule. The SVB model predicted that the electron configuration of the Au_{23} core with 14 valence electrons is expressed as $(1\Sigma)^2(1\Sigma^*)^2(1\Pi)^4(2\Sigma)^2(1\Pi^*)^4$ where each orbital is created by the bonding and antibonding interactions between the 1S and 1P superatomic orbitals of the icosahedral Au_{13} units. Therefore, the bi-icosahedral Au_{23} can be viewed as a di-superatomic molecule. To validate the SVB model, we herein conducted anion photoelectron spectroscopy (PES) on $[M_1Au_{37}(PET)_{24}]^-$ (M = Pd and Pt), which are isoelectronic and isostructural with $Au_{38}(PET)_{24}$. To this end, the neutral precursors $[M_1Au_{37}(PET)_{24}]^0$ were first synthesized by fusion reactions between hydride-doped clusters $[HAu_9(PPh_3)_8]^{2+}$ and $[M_1Au_{24}(PET)_{18}]^-$. The formation of bi-icosahedral M_1Au_{22} cores with open electronic structure in $[M_1Au_{37}(PET)_{24}]^0$ was confirmed by single-crystal X-ray diffraction analysis and electron paramagnetic resonance measurement. Then, the target anions $[M_1Au_{37}(PET)_{24}]^-$ were obtained by reducing $[M_1Au_{37}(PET)_{24}]^0$ with $NaBH_4$, and isoelectronicity with $[Au_{38}(PET)_{24}]^0$ was confirmed by optical spectroscopy and density functional theory calculations. Finally, anion PES on $[M_1Au_{37}(PET)_{24}]^-$ observed two distinctive peaks as predicted by the SVB model: one from the nearly degenerate $1\Pi^*$ orbitals and the other from the nearly degenarate 1Π and 2Σ orbitals.

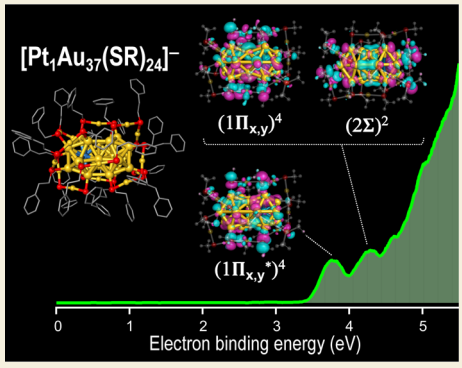

KEYWORDS: *superatomic molecules, supervalence bond (SVB) model, bi-icosahedral core, fusion-mediated synthesis, single-crystal X-ray diffraction, anion photoelectron spectroscopy, density functional theory calculation*

INTRODUCTION

Since pioneering works by Teo,[1] an increasing number of ligand-protected gold clusters with anisotropic structures have recently been reported.[2−14] Single-crystal X-ray diffraction (SCXRD) analysis revealed that their Au cores are composed of small Au cluster units that are called superatoms based on the similarity of their quantized electronic structures compared with those of conventional atoms. Table 1 lists typical examples of core structures of ligand-protected anisotropic Au clusters composed of a variety of superatomic units and bonding patterns. For instance, different types of dimer and trimer of the icosahedral Au_{13} units were formed by sharing a facet[3] or vertex atom(s).[2,5,7,9] Hydrides mediate bonding between the facets of the Au_{12} units and those of the Au_{11} units to form Au_{24} and Au_{22}, respectively.[11,12] The hydride-mediated bonding between Au_9 and Au_{11} was also found in the Au_{20} heterodimer.[10] Because the structures of the superatomic units are retained, these anisotropic clusters can be viewed as "superatomic molecules".[15−22]

The bonding theory of superatomic molecules is an interesting subject based on an analogy of the chemical bonding theory of conventional molecules.[23] A supervalence bond (SVB) model has been proposed for the bi-icosahedral Au_{23} core of a thiolate-protected Au cluster $Au_{38}(PET)_{24}$ (referred to as $\mathbf{Au_{23}}$ hereafter, PET = SC_2H_4Ph).[16,17,22] According to the SVB model, the electron configuration of $\mathbf{Au_{23}}$ with 14 electrons is expressed as $(1\Sigma)^2(1\Sigma^*)^2(1\Pi)^4(2\Sigma)^2(1\Pi^*)^4$: the 1Σ and $1\Sigma^*$ orbitals are constructed by the bonding and antibonding interactions between the 1S superatomic orbitals (SOs) of the Au_{13} units, respectively; the $1\Pi/1\Pi^*$ and $2\Sigma/2\Sigma^*$ orbitals were constructed by the tangential and coaxial overlaps of the 1P SOs of the Au_{13} units.[16,17] A comparison with conventional diatomic molecules showed that such a bonding scheme in $\mathbf{Au_{23}}$ is similar to that in F_2 molecules. The extension of this idea to $Pd_2Au_{36}(PET)_{24}$ ($\mathbf{Pd_2Au_{21}}$) with 12 electrons suggests

Received: September 19, 2022
Revised: October 14, 2022
Accepted: October 20, 2022
Published: November 4, 2022

Table 1. Examples of Au Superatomic Molecules[a]

Superatom	Bonding pattern	Superatomic molecules		Ref.
Au_{13}	Face shared	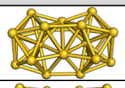	Au_{23}	3
	Vertex shared	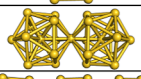	Au_{25}	2,9
		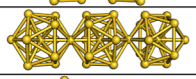	Au_{37}	5
Au_{12}	Hydride bridged	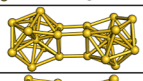	Au_{24}	12
Au_{11}	Hydride bridged	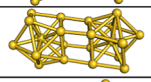	Au_{22}	11
Au_9, Au_{11}	Hydride bridged	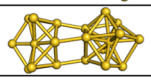	Au_{20}	10

[a]The ligand layer is omitted for simplicity.

that the ground state is triplet, similar to O_2 molecules. However, the superconducting quantum interference device (SQUID) magnetometer measurement demonstrated that **Pd_2Au_{21}** was not a triplet species but a singlet species.[24] This phenomenon was explained by the breaking of the degeneracy of the highest occupied molecular orbitals (HOMOs) by lowering the core symmetry, implying that a Hund's-type rule is not applicable for **Pd_2Au_{21}**. It was also found that the 1P SOs of the $Pd@Au_{12}$ units in **Pd_2Au_{21}** overlap in a tilted configuration.[24] Thus, the bonding theory of superatomic molecules is still in its infancy.

A promising experimental approach for validation of the SVB model is gas-phase photoelectron spectroscopy (PES) that allows us to probe the absolute energy levels and the density of states of the occupied SOs with reference to the vacuum level.[25−28] A monoanion of **Au_{23}** is an ideal target for PES because it allows mass selection prior to the PE measurement. However, a stable monoanion of **Au_{23}** could not be produced even with the strong reducing agent $NaBH_4$ because of the closed electronic structure of **Au_{23}**. To circumvent this problem, we used $[Pd_1Au_{37}(PET)_{24}]^-$ (**$Pd_1Au_{22}^-$**) and $[Pt_1Au_{37}(PET)_{24}]^-$ (**$Pt_1Au_{22}^-$**) obtained by reducing the corresponding neutrals $Pd_1Au_{37}(PET)_{24}$ (**Pd_1Au_{22}**) and $Pt_1Au_{37}(PET)_{24}$ (**Pt_1Au_{22}**), respectively: the formation of bi-icosahedral M_1Au_{22} cores with an open electronic structure in **M_1Au_{22}** was confirmed by SCXRD analysis and electron paramagnetic resonance (EPR) measurement. In addition, the isoelectronicity of **$M_1Au_{22}^-$** (M = Pd and Pt) and undoped **Au_{23}** was confirmed by optical spectroscopy and density functional theory (DFT) calculations. The PE spectra of the mass-selected **$M_1Au_{22}^-$** (M = Pd and Pt) were recorded in the gas phase. Two peaks in the PE spectra were assigned to the PE detachment from the 1Π, 2Σ, and 1Π* orbitals with the help of DFT calculations.

RESULTS AND DISCUSSION

Details of the synthesis and characterization are provided in the Materials and Method section. Neutral precursor clusters **M_1Au_{22}** (M = Pd and Pt) were synthesized using the fusion reactions between the hydride-doped Au cluster $[HAu_9(PPh_3)_8]^{2+}$ (**Au_9-H**) and the PET-protected clusters $[M_1Au_{24}(PET)_{18}]^-$ (**$M_1Au_{12}^-$**), respectively (Table 2).[29−31]

Table 2. Synthesis of M_1Au_{22} (M = Pd, Pt, and Au)

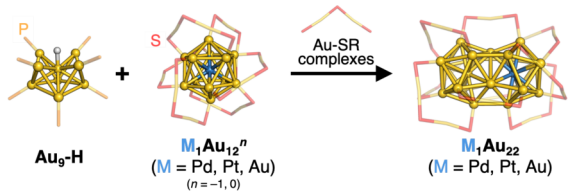

Entry	Hydride-doped clusters[a]	PET-protected clusters[b]	Isolated product: Formula[c]	Isolated product: Yield (%)
1	**Au_9-H**	**$Pd_1Au_{12}^-$**	**Pd_1Au_{22}**	17
2	**Au_9-H**	**$Pt_1Au_{12}^-$**	**Pt_1Au_{22}**	13
3	**Au_9-H**	**Au_{13}**	**Au_{23}**	11

[a]**Au_9-H**: $[HAu_9(PPh_3)_8]^{2+}$. [b]**$Pd_1Au_{12}^-$**: $[Pd_1Au_{24}(PET)_{18}]^-$, **$Pt_1Au_{12}^-$**: $[Pt_1Au_{24}(PET)_{18}]^-$, and **$Au_{13}$**: $Au_{25}(PET)_{18}$. [c]**Pd_1Au_{22}**: $Pd_1Au_{37}(PET)_{24}$, **Pt_1Au_{22}**: $Pt_1Au_{37}(PET)_{24}$, and **Au_{23}**: $Au_{38}(PET)_{24}$.

First, **Au_9-H** was prepared by adding an equal amount of $NaBH_4$ to $[Au_9(PPh_3)_8]^{3+}$.[29] Independently, **$M_1Au_{12}^-$** (M = Pd and Pt) was synthesized according to the reported methods.[24,30,31] Then, the Au(I)-PET oligomer was prepared by mixing $Au(I)ClSMe_2$ and PET with 2:1 equivalence. Finally, two DCM solutions containing the equivalent amount of **Au_9-H** and **$M_1Au_{12}^-$** (M = Pd and Pt) were mixed, followed by the addition of 6 equiv of Au(I)-PET (entries 1 and 2, Table 2). Similarly, **Au_{23}** was synthesized as a reference by the fusion reaction between **Au_9-H** and $Au_{25}(PET)_{18}$ (**Au_{13}**) (entry 3, Table 2).[32,33] The products were isolated by chromatography.

The charge state of the isolated products of entries 1−3 was assigned to be neutral because no ion signal was observed in attempts to measure the mass spectrum using electrospray ionization (ESI). Thus, they were characterized by positive-ion matrix-assisted laser desorption/ionization (MALDI) mass spectrometry (Figure 1a), EPR spectroscopy (Figure 1b), UV−vis absorption spectroscopy (Figure 1c), and SCXRD (Figure 1d, Table S1). The MALDI mass spectrum of the isolated product of entry 1 (green trace in Figure 1a) indicates the successful synthesis of **Pd_1Au_{22}**. Although the MALDI mass spectrum of the product of entry 2 (pink trace in Figure 1a) exhibits the mass peak at $m/z \sim 10770$ close to that of **Pt_1Au_{22}** (calculated m/z 10776.25), this analysis alone could not exclude the possibility of assignment to the undoped **Au_{23}** (m/z 10778.14). To facilitate the assignment, the EPR spectrum of the product of entry 2 was recorded in a frozen DCM at 5 K (Figure 1b). The EPR profiles were fitted with the following parameters: g tensor (g_1, g_2, g_3), anisotropic hyperfine coupling tensor (A_1, A_2, A_3) between two Au ($I = 3/2$) nuclei with natural abundances, and line width. The fitted parameters are listed in Table S2. The results show that both products of entries 1 and 2 are paramagnetic and have an open electronic structure, whereas **Au_{23}** is diamagnetic. Our EPR spectrum agreed well with that of **Pt_1Au_{22}** recently synthesized by a co-reduction method.[34] We conclude from these results that the products of entries 1 and 2 are assigned to **Pd_1Au_{22}** and **Pt_1Au_{22}**, respectively. The product of entry 3 was unambiguously assigned to **Au_{23}** based on the MALDI MS and the characteristic UV−vis spectrum.[35−38] Under optimized synthesis conditions, the isolated yields of **Pd_1Au_{22}**, **Pt_1Au_{22}**, and **Au_{23}** were 17, 13, and 11%, respectively, based on the amount of Pd, Pt, and Au. Synthesis of **M_1Au_{22}** (M = Pd and Pt) was

https://doi.org/10.1021/jacsau.2c00519
JACS Au 2022, 2, 2627−2634

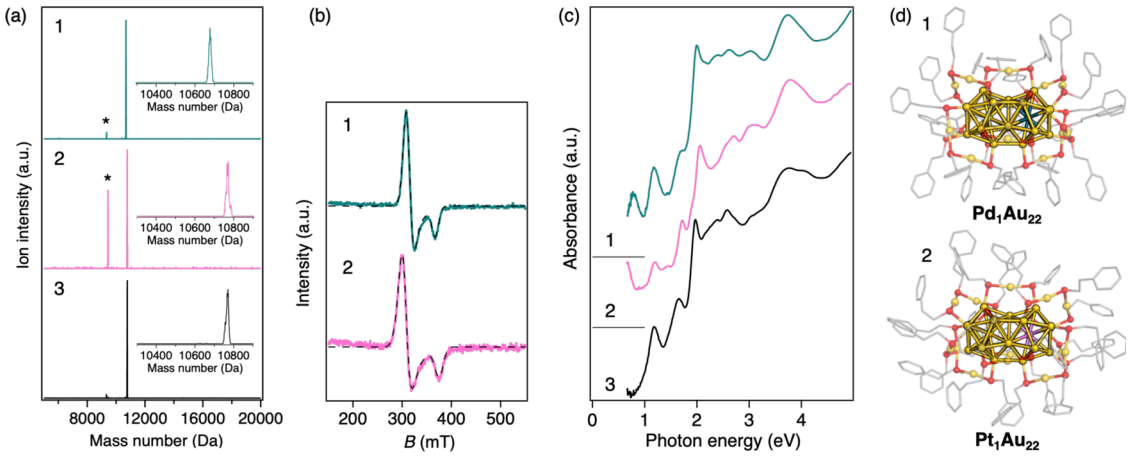

Figure 1. (a) Positive-ion MALDI mass spectra of the products of entries 1−3. Peaks with an asterisk are assigned to laser-induced fragments ($Au_4(PET)_4$ loss). The inset shows the expanded mass spectra. (b) Experimental (colored, solid) and simulated (black, dotted) X-band EPR spectra of the products of entries 1 and 2. (c) Optical absorption spectra of the products of entries 1−3 in $CHCl_3$ as a function of the photon energy. The spectra as a function of the wavelength are shown in Figure S1. (d) Crystal structures of the products of entries 1 and 2. Metal and sulfur atoms are shown as spheres. Color code: yellow, Au; teal, Pd; pink, Pt; red, S; and gray, C. Organic residues are depicted as gray sticks, and H atoms and disordered parts are omitted for clarity. In the products of entries 1 and 2, the central position is treated as half-occupancy of the Pd/Au and Pt/Au atoms, respectively.

attempted by reactions between the hydride-doped alloy clusters $[HPd_1Au_8(PPh_3)_8]^+$ (**Pd_1Au_8-H**) or $[HPt_1Au_8(PPh_3)_8]^+$ (**Pt_1Au_8-H**) and **Au_{13}**.[24,30] However, the reaction was dominated by the core growth reactions of **M_1Au_8-H** toward **M_1Au_{12}**, and the yields of **M_1Au_{22}** were lowered (Table S3). These results show that **Au_9-H** is more reactive toward the fusion reactions than **M_1Au_8-H**.[24]

The effects of Pd or Pt doping on the geometric and electronic structures were examined by comparing **M_1Au_{22}** (M = Pd and Pt) and **Au_{23}**. The optical spectra of **M_1Au_{22}** exhibited a similar profile to that of **Au_{23}**, except for an additional band at a low energy region of <1 eV (Figure 1c). The additional bands are assigned to the electronic transition to a singly occupied molecular orbital (SOMO) and are another indication of the open electronic shells. This result indicates that the electronic structures of **Au_{23}** and **M_1Au_{22}** are similar, except that the electronic shell is closed or open. The effect of Pd/Pt doping on the geometric structures was investigated by SCXRD. Figure 1d represents the SCXRD results for **Pd_1Au_{22}** and **Pt_1Au_{22}** obtained at 103 and 100 K, respectively. The absence of counterions supported that **Pd_1Au_{22}** and **Pt_1Au_{22}** are neutral in charge state and electronically open. Spin density analysis by a single-point DFT calculation of **Pd_1Au_{22}** showed that the unpaired electron was delocalized over the Pd_1Au_{22} core (Figure S2). The structures look nearly identical to that of **Au_{23}**: they are composed of bi-icosahedral $M1Au_{22}$ (M = Pd and Pt) cores protected by three $Au_1(PET)_2$ and six $Au_2(PET)_3$ oligomers.[3,24] The location of the Pd dopant in **Pd_1Au_{22}** was identified at one of the centers of two icosahedrons,[24,39] whereas that of the Pt dopant in **Pt_1Au_{22}** was not identified because Au and Pt could not be distinguished by SCXRD. Nevertheless, it is most likely that the Pt dopant occupied either the center of the bi-icosahedrons based on the previous examples in which Pt exclusively took the central site of Au superatoms.[24,30,31,34,40−45] A qualitative comparison of the geometric structures of **M_1Au_{22}** (M = Pd, Pt, and Au) is summarized in Table 3. Although a slight elongation in the interdimer distance D_{i-i} was observed, the bond lengths within

Table 3. Selected Structural Information on M_1Au_{22} (M = Pd, Pt, and Au) Cores[a]

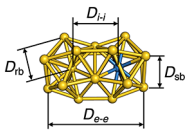

Cluster	D_{i-i}[b]	D_{e-e}[c]	D_{rb}[d]	D_{sb}[e]
Au_{23}[f]	4.087	8.427	2.751−2.835	2.756−3.025
Pd_1Au_{22}	4.094	8.433	2.744−2.833	2.758−3.126
Pt_1Au_{22}	4.112	8.453	2.743−2.814	2.797−3.030

[a]From SCXRD analysis. [b]Au−M distance in Å. [c]Averaged distance of both ends in Å. [d]Radial bond distribution of each icosahedron in Å. [e]Surface bond (<3.3 Å) distribution of each icosahedron in Å. [f]Reproduced from ref 23.

Au_{23} and **M_1Au_{22}** (M = Pd and Pt) are comparable. In summary, the structures of **M_1Au_{22}** (M = Pd and Pt) are nearly identical to that of **Au_{23}**.

Finally, **M_1Au_{22}** (M = Pd and Pt) was reduced by the reaction with $NaBH_4$.[31,46] Negative-ion ESI mass spectra after the reduction exhibit a single peak (Figure 2a). Analysis of the isotope patterns confirmed the assignment to **$M_1Au_{22}^-$**. Since the structures of **$M_1Au_{22}^-$** could not be determined by SCXRD, the structural information was obtained by optical spectroscopy and DFT calculations. The UV−vis spectra of **$M_1Au_{22}^-$** showed similar profiles with the corresponding **M_1Au_{22}** except that the lowest energy peak observed in **M_1Au_{22}** disappeared due to suppression of the optical transition to SOMO upon the reduction (Figure 2b). DFT calculations were conducted on model systems $[Pd_1Au_{37}(SCH_3)_{24}]^-$ (**$Pd_1Au_{22}(m)^-$**), $[Pt_1Au_{37}(SCH_3)_{24}]^-$ (**$Pt_1Au_{22}(m)^-$**), and $Au_{38}(SCH_3)_{24}$ (**$Au_{23}(m)$**) by simplifying PET to methane thiolate. The DFT-optimized structures are presented in Figure S3. The DFT-optimized structure of **$Au_{23}(m)$** reproduced the SCXRD structure of **Au_{23}**, demonstrating the reliability of the theoretical method used here. The optimized structures of **$M_1Au_{22}(m)^-$** were similar to the crystal structures of corresponding neutrals **M_1Au_{22}** (Figure 1d).

https://doi.org/10.1021/jacsau.2c00519
JACS Au 2022, 2, 2627−2634

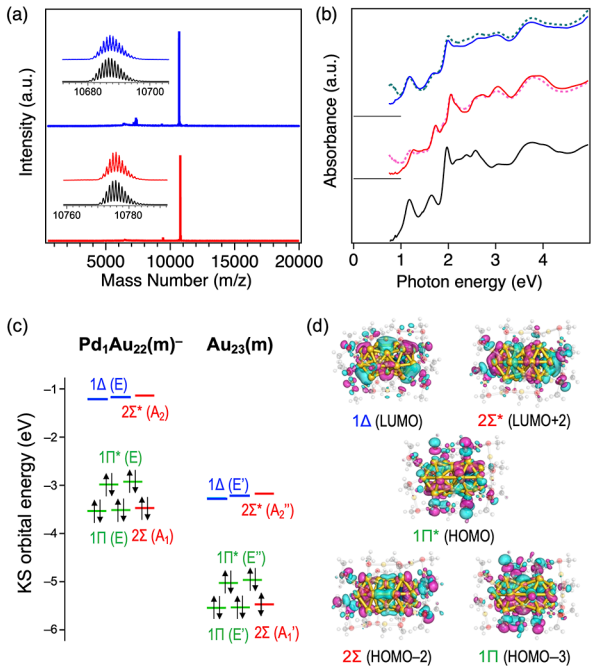

Figure 2. (a) Negative-ion ESI mass spectra. Insets compare the experimental (colored) and simulated (black) isotope patterns. (b) Comparison of UV−vis spectra of $\mathbf{Pd_1Au_{22}}^-$ (blue, solid) and $\mathbf{Pt_1Au_{22}}^-$ (red, solid) to that of $\mathbf{Au_{23}}$ (black, solid) in THF. Dotted lines show the spectra of $\mathbf{Pd_1Au_{22}}$ (green) and $\mathbf{Pt_1Au_{22}}$ (pink) before the reduction. (c) Energy diagram of the selected KS orbitals of $\mathbf{Pd_1Au_{22}(m)}^-$ (left) and $\mathbf{Au_{23}(m)}$ (right). (d) Selected KS orbitals of $\mathbf{Pd_1Au_{22}(m)}^-$. Isodensity value was set to 0.015.

These results indicate that $\mathbf{M_1Au_{22}}$ retains the geometric structures upon the reduction.

Interestingly, the spectral profiles of $\mathbf{M_1Au_{22}}^-$ are very similar to that of $\mathbf{Au_{23}}$ except for the slight blue shift for M = Pt (Figure 2b). The spectral similarity between $\mathbf{M_1Au_{22}}^-$ and $\mathbf{Au_{23}}$ is rationalized by the similar energy diagrams of their Kohn−Sham orbitals, although the KS orbitals of $\mathbf{M_1Au_{22}}^-$ are upshifted with respect to the corresponding orbitals of $\mathbf{Au_{23}}$ due to the negative charge (Figures 2c and S4). The contribution of atomic orbitals to each KS orbitals of $\mathbf{M_1Au_{22}(m)}^-$ was analyzed (see the Materials and Method section for details). The projected density of states thus obtained (Figure S5) indicates that the frontier KS orbitals are mainly composed of sp orbitals of the metals in the M_1Au_{22} core. The shapes of the frontier KS orbitals from LUMO+2 to HOMO−4 are presented in Figures S6 and S7, and selected orbitals are shown in Figure 2d. It appears that the orbitals from LUMO+2 to HOMO−4 of $\mathbf{M_1Au_{22}(m)}^-$ and $\mathbf{Au_{23}(m)}$ are divided into five types: 2Σ*, 1Δ, 1Π*, 2Σ, and 1Π. The occupied orbitals are energetically divided into two subsets (Figure 2c): (1) two 1Π* orbitals and (2) one 2Σ and two 1Π orbitals. The nature of the occupied orbitals of $\mathbf{M_1Au_{22}(m)}^-$ agrees with the theoretical prediction for $\mathbf{Au_{23}(m)}$ based on the SVB model.[16,17] The NBO charge analysis of $\mathbf{M_1Au_{22}(m)}^-$ and $\mathbf{Au_{23}(m)}$ revealed that the charge distribution is not uniform in the hetero-bi-icosahedral M_1Au_{22} core. As shown in Table S4, the charge distribution at the M_1Au_{12} side of the core of $\mathbf{M_1Au_{22}(m)}^-$ was negatively biased by ∼0.3*e* compared to the Au_{13} side because of the lower valency of Pd and Pt than Au. Nevertheless, we can conclude that the electron configurations of $\mathbf{M_1Au_{22}}^-$ (M = Pd and Pt) and $\mathbf{Au_{23}}$ are both expressed as $(1\Sigma)^2(1\Sigma^*)^2(1\Pi)^4(2\Sigma)^2(1\Pi^*)^4$.

The PE spectra of the mass-selected $\mathbf{M_1Au_{22}}^-$ (M = Pd and Pt) were recorded by a home-built apparatus consisting of an ESI source, a quadrupole linear ion trap, a time-of-flight mass spectrometer (TOF MS), and a magnetic bottle-type photoelectron spectrometer (MB PES) (Figure S8).[28] Briefly, $\mathbf{M_1Au_{22}}^-$ was introduced into the vacuum apparatus through the ESI source, was mass selected, and then was irradiated with the fourth harmonics of a Nd:YAG laser (266 nm) or the output of an ArF excimer laser (193 nm). The laser fluence was carefully adjusted to detect only a single-photon electron detachment process ($\mathbf{M_1Au_{22}}^- + h\nu \rightarrow \mathbf{M_1Au_{22}} + e^-$) and to avoid two-photon processes.[28] The detached electrons were collected by an inhomogeneous magnetic field and detected by the MB PES. The electron binding energy (E_b) was determined by subtracting the electron kinetic energy from the photon energy and then was calibrated using the PE spectra of I^-. The representative PE spectra of $\mathbf{M_1Au_{22}}^-$ (M = Pd and Pt) are shown in Figure 3a. The PE spectra of both

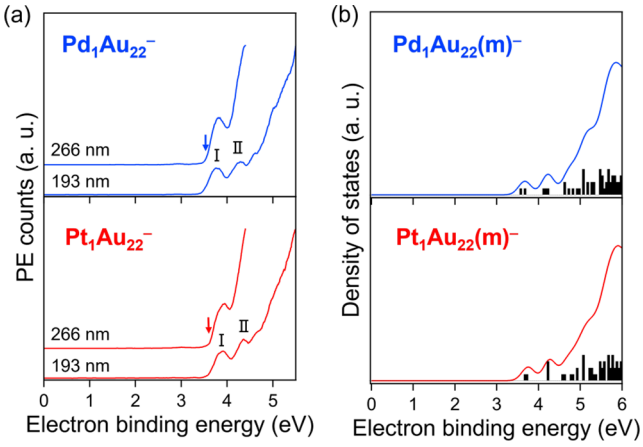

Figure 3. (a) Gas-phase PE spectra of $\mathbf{Pd_1Au_{22}}^-$ (top) and $\mathbf{Pt_1Au_{22}}^-$ (bottom). Blue and red traces at 266 nm were measured with a laser fluence of 0.5 and 1 mJ cm^{-2}, respectively. Arrows show the adiabatic electron affinities. (b) Calculated density of states of $\mathbf{Pd_1Au_{22}(m)}^-$ (top) and $\mathbf{Pt_1Au_{22}}$ $\mathbf{(m)}^-$ (bottom). Each states were broadened with a full width half-maximum of 0.35 eV.

clusters at 193 nm (1 mJ cm^{-2}) exhibited two peaks I and II centered at ∼3.8 and ∼4.3 eV along with intense broad bands at the higher E_b of >4.5 eV. The PE spectra at 266 nm showed peak I and a rising edge of peak II (Figure 3a). Based on the onset energies of peak I, the adiabatic electron affinities of $\mathbf{M_1Au_{22}}$ were determined to be 3.53 ± 0.06 and 3.60 ± 0.06 eV for M = Pd and Pt, respectively. The PE spectra of $\mathbf{M_1Au_{22}(m)}^-$ (M = Pd and Pt) were theoretically simulated by assuming the identical photoelectron detachment probability from all the states. The theoretical PE spectra shown in Figure 3b predicted that the vertical detachment energies of $\mathbf{M_1Au_{22}(m)}$ (M = Pd and Pt) were 3.64 and 3.72 eV, respectively, and reproduced the experimental spectral features shown in Figure 3a. The results of Figure 3a,b suggest that peak I is assigned to the PE detachment from nearly degenerate 1Π* orbitals, whereas peak II is assigned to that from nearly degenerate 2Σ and 1Π orbitals. These PE results support the SVB theory.

https://doi.org/10.1021/jacsau.2c00519
JACS Au 2022, 2, 2627−2634

CONCLUSIONS

In summary, a SVB model proposed for a bi-icosahedral Au_{23} core in $Au_{38}(PET)_{24}$ was tested by gas-phase PES of $[M_1Au_{37}(PET)_{24}]^-$ (M = Pd and Pt) having similar electronic structures. Targeted anions were obtained by the reduction of neutral $[M_1Au_{37}(PET)_{24}]^0$ synthesized by fusion reactions between two superatoms, $[HAu_9(PPh_3)_8]^{2+}$ and $[M_1Au_{24}(PET)_{18}]^-$. SCXRD and EPR measurements revealed that $[M_1Au_{37}(PET)_{24}]^0$ possessed open electronic structures and bi-icosahedral M_1Au_{22} cores with geometric structures similar to the bi-icosahedral Au_{23} core of $Au_{38}(PET)_{24}$. The anion photoelectron spectra of $[M_1Au_{37}(PET)_{24}]^-$ showed two peaks with the electron binding energies of ∼3.8 and ∼4.5 eV, which were assigned to the PE detachment from the 1Π* and 1Π/2Σ orbitals. This study not only demonstrates the wide applicability of the fusion reactions of superatoms for the targeted synthesis of superatomic molecules but also provides experimental support for the SVB model.

MATERIALS AND METHOD

Chemicals

All commercially available chemicals were used without further purification. Sodium borohydride ($NaBH_4$), trimethylamine (NEt_3), acetone, ethanol (EtOH), methanol (MeOH), dichloromethane (DCM), hexane, chloroform, and chlorobenzene were obtained from FujiFilm Wako Pure Chemical Corporation. 2-Phenylethanethiol (PET-H) and *trans*-2-[3-(4-*tert*-butylphenyl)-2-methyl-2-propenylidene]malononitrile (DCTB) were purchased from Tokyo Chemical Industry. Tetrahydrofuran (THF; dehydrated and stabilizer free) and DCM (dehydrated) were purchased from Kanto Chemical Company. 1, 2-Dichlorobenzene was obtained from Merck. $AuClSMe_2$ complex, $M_1Au_{24}(PET)_{18}$ (M = Pd and Pt), $[Au_9(PPh_3)_8](NO_3)_3$, $Au_{25}(PET)_{18}$, and $M_2Au_{36}(PET)_{24}$ (M = Pd and Pt) were synthesized according to the reported procedures, respectively.[24,28,30,47,48]

General Procedure

UV−vis optical spectra of the products were measured by a Jasco V-670 spectrophotometer using 2 and 10 mm cuvettes. Electrospray ionization (ESI) mass spectra were recorded on a Bruker compact ESI-Q-TOF-MS. Matrix-assisted laser desorption/ionization (MALDI) mass spectra were recorded by a Shimadzu AXIMA-CFR. DCTB was used as a matrix. The sample (0.1 mg) and DCTB (1.5 mg) were dissolved in toluene (20 μL), and a few microliters of the mixed solution were spotted on the MALDI plate. Gel permeation chromatography was conducted using a YMC-GPC T30000 column with toluene as an eluent. X-band CW-EPR measurement was carried out using a Bruker E500 spectrometer with a ^{4}He flow cryostat. The DCM solution was placed in a quartz tube (4 mmφ) and rapidly frozen by immersing in liquid N_2. The frozen solution was quickly transferred to the precooled cryostat, and measurement was conducted at several temperatures. The spectrum shown in this paper was recorded by using the following parameters: microwave frequency = 9.67 GHz, microwave power = 0.1 mW, and modulation amplitude = 0.500 mT. The microwave power dependency indicated that the condition was far less than saturation (data not shown). The EPR spectrum was simulated using the EasySpin toolbox in MATLAB 9.6.0.5. The range of 150−550 mT was used for fitting.

Synthesis

$[Pd_1Au_{37}(SC_2H_4Ph)_{24}]^0$ (Pd_1Au_{22}). A vial was charged with $Pd_1Au_{24}(PET)_{18}$ (9.1 mg, 1.25 μmol), followed by DCM (1.1 mL). Ethanolic solution containing 1 equiv of $NaBH_4$ (0.1 M, 12.5 μL) was added to the vial (solution A). $[Au_9(PPh_3)_8](NO_3)_3$ (1 equiv, 5.0 mg, 1.25 μmol) was dissolved in DCM (275 μL) in another vial, followed by the rapid addition of ethanolic solution containing 1 equiv of $NaBH_4$ (0.1 M, 12.5 μL) (solution B). Solution B was added dropwise to solution A, and the mixture was stirred at room temperature for 20 min. $AuClSMe_2$ (12 equiv, 4.4 mg, 15 μmol) was added to THF (250 μL) in another vial to obtain a white suspension. PET (6 equiv, 1.01 μL, 7.5 μmol) was added dropwise to the suspension while stirring to obtain a pale yellow solution (solution C). Solution C was added dropwise to the mixture of solutions A and B, and the mixture was stirred at room temperature for more than 130 min. Then, 12 equiv of NEt_3 (2.08 μL, 15 μmol) was added to the solution, and the mixture was stirred for 10 min. Finally, MeOH was added, and the solution was evaporated to dryness. The residue was washed with EtOH and extracted with DCM. The extract was evaporated and then purified by running Al_2O_3 column chromatography. DCM and *n*-hexane mixed in different volume ratios were used as the mobile phase. First, a column was built, and the crude product was loaded with the least polar solvent (DCM/*n*-hexane = 1:1). Then, the eluent was changed to a more polar solvent (DCM/*n*-hexane = 2:1). In the end, the most polar eluent (DCM/*n*-hexane = 6:1) was used. Green bands eluted first, and then the color of the bands gradually changed to brown. The first few fractions turning to brown were discarded because their UV−vis spectra suggested the contamination by a small amount of **Au_{23}**. The latter brown part of the bands was collected and further purified with PTLC. PTLC was developed with the mixture of DCM and *n*-hexane to obtain green and brown bands. A brown band was collected and extracted with a volume ratio of DCM/MeOH = 50:1. The brown bands were collected and dried *in vacuo*. Yield: 2.3 mg (17% with respect to Pd). The residue was recrystallized after purification with GPC.

$[Pt_1Au_{37}(SC_2H_4Ph)_{24}]^0$ (Pt_1Au_{22}). A vial was charged with $Pt_1Au_{24}(PET)_{18}$ (9.2 mg, 1.25 μmol), followed by DCM (1.1 mL). Ethanolic solution containing 1 equiv of $NaBH_4$ (0.1 M, 12.5 μL) was added to the vial (solution A′). $[Au_9(PPh_3)_8](NO_3)_3$ (1 equiv, 5.0 mg, 1.25 μmol) was dissolved in DCM (275 μL). Ethanolic solution containing 1 equiv of $NaBH_4$ (0.1 M, 12.5 μL) was rapidly added to the vial (solution B). Solution B was added dropwise to solution A′, and the mixture was stirred at room temperature for 20 min. $AuClSMe_2$ (12 equiv, 4.4 mg, 15 μmol) was put in THF (250 μL) in another vial to obtain a white suspension. PET (6 equiv, 1.01 μL, 7.5 μmol) was added dropwise to the suspension while stirring to obtain a pale yellow solution (solution C). Solution C was added dropwise to the mixture of solutions A′ and B, and the mixture was stirred at room temperature for 130 min. Then, 12 equiv of NEt_3 (2.08 μL, 15 μmol) was added to the solution, and the mixture was stirred for 10 min. Finally, MeOH was added, and the solution was evaporated to dryness. The residue was washed with EtOH and extracted with DCM. The extract was evaporated and then purified with Al_2O_3 column chromatography using the same procedure as that for **Pd_1Au_{22}**. The isolated yield was 1.8 mg (13% with respect to Pt).

$[Au_{38}(SC_2H_4Ph)_{24}]^0$ (Au_{23}). A vial was charged with $Au_{25}(PET)_{18}$ (9.2 mg, 1.25 μmol) and DCM (1.1 mL) (solution A″). In another vial, 1 equiv of $[Au_9(PPh_3)_8](NO_3)_3$ (5.0 mg, 1.25 μmol) was weighed and dissolved in DCM (275 μL). Ethanolic solution containing 1 equiv of $NaBH_4$ (0.1 M, 12.5 μL) was rapidly added to the vial (solution B). Solution B was mixed dropwise with solution A″, and the mixture was stirred at room temperature for 20 min. $AuClSMe_2$ (12 equiv, 4.4 mg, 15 μmol) was prepared in the third vial to which THF (250 μL) was added to make a white suspension. PET (6 equiv, 1.01 μL, 7.5 μmol) was added dropwise to the suspension while stirring to obtain a pale yellow solution (solution C). Solution C was added dropwise to the mixture of solutions A″ and B, and the mixture was stirred at room temperature for more than 100 min. Then, 12 equiv of NEt_3 (2.08 μL, 15 μmol) was added to the solution, and the mixture was stirred for 10 min. Finally, MeOH was added, and the solution was evaporated to dryness. The residue was washed with EtOH and subsequently extracted with DCM. The extract was evaporated and then purified using silica gel column chromatography. The mixtures of DCM and *n*-hexane with a 1:1 volume ratio were used as an eluent. The brown band was collected and dried *in vacuo*. Yield: 1.8 mg (11% with respect to Au).

https://doi.org/10.1021/jacsau.2c00519
JACS Au 2022, 2, 2627−2634

X-ray Crystallography

General. The crystals were gradually cooled by a cold N_2 stream at ~10 K/min to minimize the structural disorder in the ligand shells. Diffraction experiments were performed using a Rigaku VariMax dual diffractometer with a Pilatus 200K hybrid pixel array detector with MoKα radiation. The data were corrected for Lorentz polarization, and the absorption correction was performed numerically using the CrysAlisPro software. The initial phase trials were conducted by a direct method using SHELXS-2014, and the structures were refined using the full-matrix least-squares method on F^2 by SHELXL-2018.[49] All non-hydrogen atoms, except for the solvent molecule, were refined anisotropically, and the hydrogen atoms were treated as riding models. All aromatic rings were treated using rigid constraints (AFIX 66). Disordered organic residues in the ligands were treated by splitting the moieties into several parts to build a reasonable model. Special treatment for structure refinement, CheckCif reports, Cambridge Crystallographic Data Center (CCDC) depository numbers, and structural notes are listed as follows.

Pd_1Au_{22}. Crystals for X-ray diffraction experiments were prepared by mixing a chlorobenzene solution of clusters (~10 mg/mL) and *n*-hexane with a volume ratio of 1:7 in a test tube at room temperature for 1 week. Since the cluster consists of one Pd atom, the sum of half-occupancy of Pd atom and Au atom at the center of the icosahedron was assumed for the refinement using the same positional and displacement factors of each elements. The CheckCIF program did not generate any A and B level alerts (CCDC depository no. 2194621).

Pt_1Au_{22}. Crystals for X-ray diffraction experiments were prepared by mixing a 1,2-dichlorobenzene solution of clusters (~10 mg/mL) and *n*-hexane with a volume ratio of 1:7 in a test tube at room temperature for 3 weeks during which *n*-hexane was added several times. The half-occupancy of Pt atoms at the center of each icosahedrons was assumed. The CheckCIF program generated B level alerts regarding some missing reflections below theta(min) and relatively high residual electron densities. The former is due to the interference of the direct beam stopper caused by MoKα radiation with low crystal symmetry. The latter is due to an imperfect absorption correction derived from the anisotropic crystal shape and highly disordered nature of the crystal. Although these alerts were found, the conclusion was not affected by these alerts since the total structural motif is unequivocal (CCDC depository no. 2194620).

Gas-Phase PES

PES was conducted using a custom-built apparatus equipped with an electrospray ionization (ESI) source, a time-of-flight mass spectrometer (TOF-MS), and a magnetic-bottle-type photoelectron spectrometer (MB-PES) (Figure S8).[28] $\mathbf{M_1Au_{22}}^-$ was prepared by reducing 0.2 mg of $\mathbf{M_1Au_{22}}$ dissolved in THF (20 μL) with 1 equiv of $NaBH_4$ dissolved in cold EtOH (0.01 M, 1.86 μL) and then diluted with THF (1 mL). $\mathbf{M_1Au_{22}}^-$ was introduced into the apparatus *via* the ESI source and desolvated by a heated capillary. Ions were transferred to a linear quadrupole ion trap (LQT) through a skimmer (1 mm diameter). Continuously flowing ions were accumulated in the LQT for 99 ms and released 300 μs before the acceleration of the TOF-MS. The released ions were accelerated by a set of Wiley−McLaren-type electrodes and were temporally and spatially separated by the TOF-MS with a mass resolution ($\Delta m/m$) of ~600. Pulsed third or fourth harmonics of an Nd:YAG nanosecond laser (Quanta-Ray GCR130, Spectra-Physics, US) or pulsed ArF excimer laser (PSX-100, MPB Communications Inc.) clipped by a pinhole were irradiated to the mass-selected ion beam during the TOF-MS. The emitted photoelectrons were collected by an inhomogeneous magnetic field generated by a permanent magnet and a coil. The kinetic energies of the photoelectrons were determined by the TOF of the electrons and then converted to the electron binding energies (EBEs). The EBEs were calibrated with the PE spectrum of I^- produced by the dissociative electron attachment to CH_3I. The energy resolution was approximately 110 mV for an electron with a kinetic energy of 1 eV. The obtained PE spectra were smoothed by averaging the data points within ±50 meV. The adiabatic electron affinity was determined by the energy of the spectral onset where the tangential line at the inflection point intersected the *X*-axis. Laser fluences were measured at the exit of the Nd:YAG laser.

DFT Calculations

Density functional theory (DFT) calculation was conducted on $Au_{38}(SCH_3)_{24}^0$ ($\mathbf{Au_{23}(m)}$), $[Pd_1Au_{37}(SCH_3)_{24}]^-$ ($\mathbf{Pd_1Au_{22}(m)^-}$), and $[Pt_1Au_{37}(SCH_3)_{24}]^-$ ($\mathbf{Pt_1Au_{22}(m)^-}$) with B3LYP functionals and 6-31G(d) basis sets for H, C, and S atoms and LanL2DZ basis sets for Pd, Pt, and Au atoms by using the Gaussian 16 program.[50] All structures were created from crystal structures by substituting the PET ligands with SCH_3 and structural optimization was performed. Frequency calculations on the optimized structures did not show any imaginary frequencies, indicating that the obtained structures were at local minima. Vertical detachment energies were calculated by subtracting the total energy of the structure-optimized $\mathbf{Pd_1Au_{22}(m)^-}$ and $\mathbf{Pt_1Au_{22}(m)^-}$ from that of the neutrals with the fixed geometries without considering the zero-point energies. Spin density of $\mathbf{Pd_1Au_{22}}$ was examined by single-point calculation on the crystal structure at the same level of calculations. The contributions of atomic orbitals to each Kohn−Sham orbital were analyzed based on Mulliken population analysis (MPA) using the GaussSum program.[51] NBO charge analysis was conducted by the NBO program implemented in the Gaussian.[52]

■ ASSOCIATED CONTENT

Supporting Information

The Supporting Information is available free of charge at https://pubs.acs.org/doi/10.1021/jacsau.2c00519.

Optical absorption spectra of the products of entries 1−3 in Table 2; KS orbitals of $\mathbf{Pd_1Au_{22}(m)^-}$, $\mathbf{Pt_1Au_{22}(m)^-}$, and $\mathbf{Au_{23}(m)}$; schematic illustration of the PES apparatus; fitting results of EPR data; synthetic results; and crystal data (PDF).

$C_{204}H_{235}Au_{37}ClPdS_{24}$ (CIF)

$C_{192}H_{216}Au_{37}PtS_{24}$ (CIF)

$PtAu_{37}PET_{24}$ at 100 K (PDF)

$PdAu_{37}PET_{24}$ at 103 K (PDF)

■ AUTHOR INFORMATION

Corresponding Author

Tatsuya Tsukuda − *Department of Chemistry, Graduate School of Science, The University of Tokyo, Tokyo 113-0033, Japan;* orcid.org/0000-0002-0190-6379; Email: tsukuda@chem.s.u-tokyo.ac.jp

Authors

Emi Ito − *Department of Chemistry, Graduate School of Science, The University of Tokyo, Tokyo 113-0033, Japan*

Shun Ito − *Department of Chemistry, Graduate School of Science, The University of Tokyo, Tokyo 113-0033, Japan*

Shinjiro Takano − *Department of Chemistry, Graduate School of Science, The University of Tokyo, Tokyo 113-0033, Japan;* orcid.org/0000-0001-9262-5283

Toshikazu Nakamura − *Institute for Molecular Science, Okazaki 444-8585, Japan;* orcid.org/0000-0001-8672-0946

Complete contact information is available at: https://pubs.acs.org/10.1021/jacsau.2c00519

Author Contributions

E.I. and S.I. equally contributed to the work. E.I. conducted the synthesis and basic characterization. S.I. conducted PES measurement and DFT calculations. S.T. advised on the

https://doi.org/10.1021/jacsau.2c00519
JACS Au 2022, 2, 2627−2634

synthesis and conducted SCXRD analysis. T.N. conducted EPR measurement. T.T. conceived the idea and supervised the project. The manuscript was drafted by E.I., S.I., and T.T. and was approved by all the authors. CRediT: **Emi Ito** data curation, formal analysis, investigation, visualization, writing-original draft; **Shun Ito** data curation, formal analysis, investigation, methodology, visualization, writing-review & editing; **Shinjiro Takano** data curation, methodology, supervision, validation, writing-review & editing; **Toshikazu Nakamura** investigation, writing-original draft; **Tatsuya Tsukuda** conceptualization, supervision, validation, visualization, writing-original draft, writing-review & editing.

Notes

The authors declare no competing financial interest.

■ ACKNOWLEDGMENTS

This research was financially supported by JST, CREST (grant no. JPMJCR20B2), and JSPS KAKENHI (grant nos. JP20H00370 and JP21J20631). Part of theoretical calculations was performed using the Research Center for Computational Science, Okazaki, Japan. Part of this work was conducted at Institute for Molecular Science, supported by nanotechnology platform program <molecule and material synthesis> (JPMXP09S20MS1047) of the Ministry of Education, Culture, Sports, Science and Technology (MEXT), Japan.

■ REFERENCES

(1) Teo, B. K.; Zhang, H. Polyicosahedricity: Icosahedron to Icosahedron of Icosahedra Growth Pathway for Bimetallic (Au-Ag) and Trimetallic (Au-Ag-M; M = Pt, Pd, Ni) Supraclusters; Synthetic Strategies, Site Preference, and Stereochemical Principles. *Coord. Chem. Rev.* **1995**, *143*, 611−636.

(2) Shichibu, Y.; Negishi, Y.; Watanabe, T.; Chaki, N. K.; Kawaguchi, H.; Tsukuda, T. Biicosahedral Gold Clusters $[Au_{25}(PPh_3)_{10}(SC_nH_{2n+1})_5Cl_2]^{2+}$ (n = 2−18): A Stepping Stone to Cluster-Assembled Materials. *J. Phys. Chem. C* **2007**, *111*, 7845−7847.

(3) Qian, H.; Eckenhoff, W. T.; Zhu, Y.; Pintauer, T.; Jin, R. Total Structure Determination of Thiolate-Protected Au_{38} Nanoparticles. *J. Am. Chem. Soc.* **2010**, *132*, 8280−8281.

(4) Wan, X.-K.; Lin, Z.-W.; Wang, Q.-M. Au_{20} Nanocluster Protected by Hemilabile Phosphines. *J. Am. Chem. Soc.* **2012**, *134*, 14750−14752.

(5) Jin, R.; Liu, C.; Zhao, S.; Das, A.; Xing, H.; Gayathri, C.; Xing, Y.; Rosi, N. L.; Gil, R. R.; Jin, R. Tri-icosahedral Gold Nanocluster $[Au_{37}(PPh_3)_{10}(SC_2H_4Ph)_{10}X_2]^+$: Linear Assembly of Icosahedral Building Blocks. *ACS Nano* **2015**, *9*, 8530−8536.

(6) Takano, S.; Yamazoe, S.; Koyasu, K.; Tsukuda, T. Slow-reduction Synthesis of a Thiolate-protected One-dimensional Gold Cluster Showing an Intense Near-infrared Absorption. *J. Am. Chem. Soc.* **2015**, *137*, 7027−7030.

(7) Song, Y.; Fu, F.; Zhang, J.; Chai, J.; Kang, X.; Li, P.; Li, S.; Zhou, H.; Zhu, M. The Magic Au_{60} Nanoclusters: A New Cluster-Assembled Material with Five Au_{13} Building Units. *Angew. Chem., Int. Ed.* **2015**, *54*, 8430−8434.

(8) Jin, S.; Du, W.; Wang, S.; Kang, X.; Chen, M.; Hu, D.; Chen, S.; Zou, X.; Sun, G.; Zhu, M. Thiol-Induced Synthesis of Phosphine-Protected Gold Nanoclusters with Atomic Precision and Controlling the Structure by Ligand/Metal Engineering. *Inorg. Chem.* **2017**, *56*, 11151−11159.

(9) Shen, H.; Deng, G.; Kaappa, S.; Tan, T.; Han, Y.-Z.; Malola, S.; Lin, S.-C.; Teo, B. K.; Häkkinen, H.; Zheng, N. Highly Robust but Surface-Active: An N-Heterocyclic Carbene-Stabilized Au_{25} Nanocluster. *Angew. Chem., Int. Ed.* **2019**, *58*, 17731−17735.

(10) Yuan, S.-F.; Li, J.-J.; Guan, Z.-J.; Lei, Z.; Wang, Q.-M. Ultrastable Hydrido Gold Nanoclusters with the Protection of Phosphines. *Chem. Commun.* **2020**, *56*, 7037−7040.

(11) Dong, J.; Gao, Z.-H.; Zhang, Q.-F.; Wang, L.-S. The Synthesis, Bonding, and Transformation of a Ligand-Protected Gold Nanohydride Cluster. *Angew. Chem., Int. Ed.* **2021**, *60*, 2424−2430.

(12) Kulkarni, V. K.; Khiarak, B. N.; Takano, S.; Malola, S.; Albright, E. L.; Levchenko, T. I.; Aloisio, M. D.; Dinh, C.-T.; Tsukuda, T.; Häkkinen, H.; Crudden, C. M. N-Heterocyclic Carbene-Stabilized Hydrido Au_{24} Nanoclusters- Synthesis, Structure, and Electrocatalytic Reduction of CO_2. *J. Am. Chem. Soc.* **2022**, *144*, 9000−9006.

(13) Shigeta, T.; Takano, S.; Tsukuda, T. A Face-to-Face Dimer of Au_3 Superatoms Supported by Interlocked Tridentate Scaffolds Formed in $Au_{18}S_2(SR)_{12}$. *Angew. Chem., Int. Ed.* **2022**, *61*, No. e202113275.

(14) Li, Y.; Song, Y.; Zhang, X.; Liu, T.; Xu, T.; Wang, H.; Jiang, D. E.; Jin, R. Atomically Precise Au_{42} Nanorods with Longitudinal Excitons for an Intense Photothermal Effect. *J. Am. Chem. Soc.* **2022**, *144*, 12381−12389.

(15) Nobusada, K.; Iwasa, T. Oligomeric Gold Clusters with Vertex-Sharing Bi- and Triicosahedral Structures. *J. Phys. Chem. C* **2007**, *111*, 14279−14282.

(16) Cheng, L.; Ren, C.; Zhang, X.; Yang, J. New Insight into the Electronic Shell of $Au_{38}(SR)_{24}$: A Superatomic Molecule. *Nanoscale* **2013**, *5*, 1475−1478.

(17) Cheng, L.; Yang, J. Communication: New Insight into Electronic Shells of Metal Clusters: Analogues of Simple Molecules. *J. Chem. Phys.* **2013**, *138*, 141101.

(18) Nishigaki, J.; Koyasu, K.; Tsukuda, T. Chemically-Modified Gold Superatoms and Superatomic Molecules. *Chem. Rec.* **2014**, *14*, 897−909.

(19) Tlahuice-Flores, A.; Muñoz-Castro, A. Bonding and Properties of Superatoms. Analogs to Atoms and Molecules and Related Concepts from Superatomic Clusters. *Int. J. Quantum Chem.* **2019**, *119*, No. e25756.

(20) Munos-Castro, A. Single, Double, and Triple Intercluster Bonds: Analyses of $M_2Au_{36}(SR)_{24}$ (M = Au, Pd, Pt) as 14-, 12- and 10-ve Superatomic Molecules. *Chem. Commun.* **2019**, *55*, 7307−7310.

(21) Omoda, T.; Takano, S.; Tsukuda, T. Toward Controlling the Electronic Structures of Chemically Modified Superatoms of Gold and Silver. *Small* **2021**, *17*, 2001439.

(22) Xu, C.; Zhou, Y.; Yi, J.; Li, D.; Shi, L.; Cheng, L. Tri- and Tetra-superatomic Molecules in Ligand-Protected Face-Fused Icosahedral $(M@Au_{12})_n$ (M = Au, Pt, Ir, and Os, and n = 3 and 4) Clusters. *J. Phys. Chem. Lett.* **2022**, *13*, 1931−1939.

(23) Mingos, D. M. P. Structural and Bonding Patterns in Gold Clusters. *Dalton Trans.* **2015**, *44*, 6680−6695.

(24) Ito, E.; Takano, S.; Nakamura, T.; Tsukuda, T. Controlled Dimerization and Bonding Scheme of Icosahedral $M@Au_{12}$ (M = Pd, Pt) Superatoms. *Angew. Chem., Int. Ed.* **2021**, *60*, 645−649.

(25) Hirata, K.; Tomihara, R.; Kim, K.; Koyasu, K.; Tsukuda, T. Characterization of Chemically Modified Gold and Silver Clusters in Gas Phase. *Phys. Chem. Chem. Phys.* **2019**, *21*, 17463−17474.

(26) Veenstra, A. P.; Monzel, L.; Baksi, A.; Czekner, J.; Lebedkin, S.; Schneider, E. K.; Pradeep, T.; Unterreiner, A.-N.; Kappes, M. M. Ultrafast Intersystem Crossing in Isolated $Ag_{29}(BDT)_{12}^{3-}$ Probed by Time-Resolved Pump−Probe Photoelectron Spectroscopy. *J. Phys. Chem. Lett.* **2020**, *11*, 2675−2681.

(27) Koyasu, K.; Tsukuda, T. Gas Phase Studies on Chemically Synthesized Au and Ag Clusters. *J. Chem. Phys.* **2021**, *154*, 140901.

(28) Ito, S.; Tasaka, Y.; Nakamura, K.; Fujiwara, Y.; Hirata, K.; Koyasu, K.; Tsukuda, T. Electron Affinities of Ligated Icosahedral M_{13} Superatoms Revisited by Gas-Phase Anion Photoelectron Spectroscopy. *J. Phys. Chem. Lett.* **2022**, *13*, 5049−5055.

(29) Takano, S.; Hirai, H.; Muramatsu, S.; Tsukuda, T. Hydride-Doped Gold Superatom $(Au_9H)^{2+}$: Synthesis, Structure and Transformation. *J. Am. Chem. Soc.* **2018**, *140*, 8380−8383.

(30) Takano, S.; Ito, S.; Tsukuda, T. Efficient and Selective Conversion of Phosphine-Protected $(MAu_8)^{2+}$ (M = Pd, Pt) Superatoms to Thiolate-Protected $(MAu_{12})^{6+}$ or Alkynyl-Protected $(MAu_{12})^{4+}$ Superatoms via Hydride Doping. *J. Am. Chem. Soc.* **2019**, *141*, 15994−16002.

https://doi.org/10.1021/jacsau.2c00519
JACS Au 2022, 2, 2627−2634

(31) Suyama, M.; Takano, S.; Nakamura, T.; Tsukuda, T. Stoichiometric Formation of Open-Shell $[PtAu_{24}(SC_2H_4Ph)_{18}]^-$ via Spontaneous Electron Proportionation between $[PtAu_{24}(SC_2H_4Ph)_{18}]^{2-}$ and $[PtAu_{24}(SC_2H_4Ph)_{18}]^0$. *J. Am. Chem. Soc.* **2019**, *141*, 14048−14051.
(32) Heaven, M. W.; Dass, A.; White, P. S.; Holt, K. M.; Murray, R. W. Crystal Structure of the Gold Nanoparticle $[N(C_8H_{17})_4]$-$[Au_{25}(SCH_2CH_2Ph)_{18}]$. *J. Am. Chem. Soc.* **2008**, *130*, 3754−3755.
(33) Zhu, M.; Aikens, C. M.; Hollander, F. J.; Schatz, G. C.; Jin, R. Correlating the Crystal Structure of A Thiol-Protected Au_{25} Cluster and Optical Properties. *J. Am. Chem. Soc.* **2008**, *130*, 5883−5885.
(34) Liu, X.; Wang, E.; Zhou, M.; Wan, Y.; Zhang, Y.; Liu, H.; Zhao, Y.; Li, J.; Gao, Y.; Zhu, Y. Asymmetrically Doping a Platinum Atom into a Au_{38} Nanocluster for Changing the Electron Configuration and Reactivity in Electrocatalysis. *Angew. Chem., Int. Ed.* **2022**, *61*, No. e202207685.
(35) Chaki, N. K.; Negishi, Y.; Tsunoyama, H.; Shichibu, Y.; Tsukuda, T. Ubiquitous 8 and 29 kDa Gold: Alkanethiolate Cluster Compounds: Mass-Spectrometric Determination of Molecular Formulas and Structural Implications. *J. Am. Chem. Soc.* **2008**, *130*, 8608−8610.
(36) Dolamic, I.; Knoppe, S.; Dass, A.; Bürgi, T. First Enantioseparation and Circular Dichroism Spectra of Au_{38} Clusters Protected by Achiral Ligands. *Nat. Commun.* **2012**, *3*, 798.
(37) Qian, H.; Zhu, Y.; Jin, R. Size-Focusing Synthesis, Optical and Electrochemical Properties of Monodisperse $Au_{38}(SC_2H_4Ph)_{24}$ Nanoclusters. *ACS Nano* **2009**, *3*, 3795−3803.
(38) Dainese, T.; Antonello, S.; Bogialli, S.; Fei, W.; Venzo, A.; Maran, F. Gold Fusion: From $Au_{25}(SR)_{18}$ to $Au_{38}(SR)_{24}$, the Most Unexpected Transformation of a Very Stable Nanocluster. *ACS Nano* **2018**, *12*, 7057−7066.
(39) Negishi, Y.; Igarashi, K.; Munakata, K.; Ohgake, W.; Nobusada, K. Palladium Doping of Magic Gold Cluster $Au_{38}(SC_2H_4Ph)_{24}$: Formation of $Pd_2Au_{36}(SC_2H_4Ph)_{24}$ with Higher Stability Than $Au_{38}(SC_2H_4Ph)_{24}$. *Chem. Commun.* **2012**, *48*, 660−662.
(40) Qian, H.; Jiang, D.-e.; Li, G.; Gayathri, C.; Das, A.; Gil, R. R.; Jin, R. Monoplatinum Doping of Gold Nanoclusters and Catalytic Application. *J. Am. Chem. Soc.* **2012**, *134*, 16159−16162.
(41) Kwak, K.; Tang, Q.; Kim, M.; Jiang, D.-e.; Lee, D. Interconversion between Superatomic 6-Electron and 8-Electron Configuration of $M@Au_{24}(SR)_{18}$ Clusters (M = Pd, Pt). *J. Am. Chem. Soc.* **2015**, *137*, 10833−10840.
(42) Tian, S.; Liao, L.; Yuan, J.; Yao, C.; Chen, J.; Yang, J.; Wu, J. Structures and Magnetism of Mono-Palladium and Mono-Platinum Doped $Au_{25}(PET)_{18}$ Nanoclusters. *Chem. Commun.* **2016**, *52*, 9873−9876.
(43) Kim, M.; Tang, Q.; Kumar, A. V. N.; Kwak, K.; Choi, W.; Jiang, D.-e.; Lee, D. Dopant-Dependent Electronic Structures Observed for $M_2Au_{36}(SC_6H_{13})_{24}$ Clusters (M = Pt, Pd). *J. Phys. Chem. Lett.* **2018**, *9*, 982−989.
(44) Fei, W.; Antonello, S.; Dainese, T.; Dolmella, A.; Lahtinen, M.; Rissanen, K.; Venzo, A.; Maran, F. Metal Doping of $Au_{25}(SR)_{18}^-$ Clusters: Insights and Hindsights. *J. Am. Chem. Soc.* **2019**, *141*, 16033−16045.
(45) Hirai, H.; Takano, S.; Nakashima, T.; Iwasa, T.; Taketsugu, T.; Tsukuda, T. Doping-Mediated Energy-Level Engineering of $M@Au_{12}$ Superatoms (M = Pd, Pt, Rh, Ir) for Efficient Photoluminescence and Photocatalysis. *Angew. Chem., Int. Ed.* **2022**, *61*, No. e202207290.
(46) Negishi, Y.; Chaki, N. K.; Shichibu, Y.; Whetten, R. L.; Tsukuda, T. Origin of Magic Stability of Thiolated Gold Clusters: A Case Study on $Au_{25}(SC_6H_{13})_{18}$. *J. Am. Chem. Soc.* **2007**, *129*, 11322−11323.
(47) Brandys, M.-C.; Jennings, M. C.; Puddephatt, R. J. Luminescent Gold(I) Macrocycles with Diphosphine and 4,4'-Bipyridyl Ligands. *J. Chem. Soc. Dalton Trans.* **2000**, 4601−4606.
(48) Tofanelli, M. A.; Salorinne, K.; Ni, T. W.; Malola, S.; Newell, B.; Phillips, B.; Häkkinen, H.; Ackerson, C. J. Jahn-Teller Effects in $Au_{25}(SR)_{18}$. *Chem. Sci.* **2016**, *7*, 1882−1890.
(49) Sheldrick, G. M. Crystal Structure Refinement with SHELXL. *Acta Crystallogr., Sect. C: Cryst. Struct. Commun.* **2015**, *71*, 3−8.
(50) Frisch, M. J.; Trucks, G. W.; Schlegel, H. B.; Scuseria, G. E.; Robb, M. A.; Cheeseman, J. R.; Scalmani, G.; Barone, V.; Petersson, G. A.; Nakatsuji, H.; Li, X.; Caricato, M.; Marenich, A. V.; Bloino, J.; Janesko, B. G.; Gomperts, R.; Mennucci, B.; Hratchian, H. P.; Ortiz, J. V.; Izmaylov, A. F.; Sonnenberg, J. L.; Williams-Young, D.; Ding, F.; Lipparini, F.; Egidi, F.; Goings, J.; Peng, B.; Petrone, A.; Henderson, T.; Ranasinghe, D.; Zakrzewski, V. G.; Gao, J.; Rega, N.; Zheng, G.; Liang, W.; Hada, M.; Ehara, M.; Toyota, K.; Fukuda, R.; Hasegawa, J.; Ishida, M.; Nakajima, T.; Honda, Y.; Kitao, O.; Nakai, H.; Vreven, T.; Throssell, K.; Montgomery, J. A., Jr.; Peralta, J. E.; Ogliaro, F.; Bearpark, M. J.; Heyd, J. J.; Brothers, E. N.; Kudin, K. N.; Staroverov, V. N.; Keith, T. A.; Kobayashi, R.; Normand, J.; Raghavachari, K.; Rendell, A. P.; Burant, J. C.; Iyengar, S. S.; Tomasi, J.; Cossi, M.; Millam, J. M.; Klene, M.; Adamo, C.; Cammi, R.; Ochterski, J. W.; Martin, R. L.; Morokuma, K.; Farkas, O.; Foresman, J. B.; Fox, D. J. *Gaussian 16*; Revision B.01, Gaussian, Inc., Wallingford CT, 2016.
(51) O'Boyle, N. M.; Tenderholt, A. L.; Langner, K. M. Cclib: A Library for Package-Independent Computational Chemistry Algorithms. *J. Comput. Chem.* **2008**, *29*, 839−845.
(52) Glendening, E. D.; Reed, A. E.; Carpenter, J. E.; Weinhold, F. *NBO*; version 3.1.

https://doi.org/10.1021/jacsau.2c00519
JACS Au 2022, 2, 2627−2634